Segmental and Chain Dynamics of Isotactic Polypropylene Melts

Georgia Evangelia Logotheti and Doros N. Theodorou*

School of Chemical Engineering, Department of Materials Science and Engineering, National Technical University of Athens, 9 Heroon Polytechniou Street, Zografou Campus, 15780 Athens, Greece

Received September 26, 2006; Revised Manuscript Received January 17, 2007

ABSTRACT: The properties of isotactic polypropylene (iPP) melts are investigated via atomistic molecular dynamics (MD) simulations in the isothermal−isobaric (*NPT*) ensemble. A fully flexible model is developed and validated by comparing predicted volumetric and thermodynamic behavior with available experimental data. Atomic-level packing in the simulated polymer melt is examined through the calculation of an X-ray diffraction pattern. Segmental dynamics is investigated through the reorientation of the methylene C−H bonds and the decorrelation function of torsion angles over a wide range of temperatures and pressures. Predicted correlation times are in reasonable agreement with experimental values derived from ^{13}C NMR, QENS, and dielectric spectroscopy measurements. The temperature (T) and pressure (P) effects on the relaxation times are compared by calculating the E_V^*/H^* ratio, which provides a quantitive measure of the relative importance of P and T on the dynamics. By consistently mapping the atomistic trajectories onto the Rouse model, the dynamical behavior of the polymer on the chain level is investigated. Estimates of the segmental friction factor are derived from both the self-diffusion coefficient and the relaxation times of the first Rouse modes. The zero-shear viscosity is calculated from the friction factor through the Rouse model analysis.

1. Introduction

Predicting the physical properties of polymeric materials from their detailed chemical constitution through atomistic simulations is of substantial importance, since it can play a significant role in the design of new materials and the improvement of their processability. Using as input information on molecular geometry and interaction potentials and taking into account the macroscopic constraints imposed on a system, molecular simulation techniques can predict static and dynamic properties, at the same time offering valuable insight into the microscopic structure and motion and into the mechanisms that underlie macroscopic behavior.

Polypropylene (PP) is a vinyl polymer with a wide variety of applications. In its most common isotactic form (iPP) it can be used as both plastic and fiber; it is unusually resistant to many chemical solvents and can be melted and recycled.

PP has been studied using several simulation techniques, such as molecular mechanics,[1−3] molecular dynamics,[4−10] and Monte Carlo[11−17] in order to predict its elastic constants in the glassy state, its volumetric, thermodynamic, conformational, and dynamical properties in the melt, and furthermore the miscibility of melts of different tacticities. A coarse-grained model based on the next-nearest-neighbor diamond lattice, the bead−spring model, united atom, and explicit atom representations have been used for PP, depending on the properties and mechanisms that needed to be explored. Dynamical simulation results available in the literature focus mainly on segmental and not on chain dynamics. Furthermore, the effect of pressure on volumetric and dynamical properties has not been investigated.

In this work we present results from atomistic molecular dynamics simulations carried out in the isothermal−isobaric (*NPT*) ensemble to study the properties of iPP polymer melts. Our objective is to investigate the dynamical behavior both at the segmental and at the chain level. Results for the segmental motion will be presented over a wide range of temperatures and pressures, in order to assess the relative importance of P and T on the dynamics. At the chain level, simulation results will be used to test the validity of the Rouse model analysis, which has been extensively used to describe chain dynamics in the unentangled regime.[18−23]

This paper is organized as follows. Section 2 discusses the molecular model invoked in the present atomistic MD simulations and explains the key points of the simulation methodology adopted. Results from the MD simulations are presented and compared with available experiments for iPP melts in section 3. Our conclusions from this work are drawn in section 4.

2. Molecular Model and Simulation Methodology

In this work, following refs 6 and 7, polypropylene chains are represented in terms of explicit skeletal carbon (C) and pendant hydrogen (H) atoms, while a united atom representation is used for the methyl groups (CH_3 = R). Two model systems were studied—one consisted of 2 and the second of 16 molecules of degree of polymerization 76 (152 skeletal bonds long, molar mass 3208 g mol^{-1})—in a cubic simulation cell[6,7] subject to periodic boundary conditions in all three directions.

In contrast to refs 6 and 7, a fully flexible (constraint-free) model is used. A simple harmonic potential keeps bond lengths b_{ij} near their equilibrium values:

$$V_{ij}^b = c_{ij}^b(b_{ij} - b_{ij}^0)^2 \tag{1}$$

with $2c_{ij}^b$ and b_{ij}^0 being the spring constants and the equilibrium bond lengths, respectively, for the three different types of bonds present in the iPP molecule.

A potential of the same form is also used in order to describe the interactions associated with all eight types of skeletal bond angles

$$V_{ijk}^\theta = c_{ijk}^\theta(\theta_{ijk} - {}^0_{\theta ijk})^2 \tag{2}$$

A 3-fold symmetric torsional potential is associated with all nonterminal dihedral angles

$$V_{ijkl}^\phi = \frac{1}{2}c_{ijkl}^\phi[1 - \cos(3\phi_{ijkl})] \tag{3}$$

* To whom correspondence should be addressed: Tel +30 210 772 3157, Fax +30 210 772 3112, e-mail doros@central.ntua.gr.

10.1021/ma062234u CCC: $37.00
Published on Web 02/27/2007

Table 1. Simulation Parameters for Bonded Interactions

bonds	CH			CC			CR		
c_{ij}^b (kJ mol^{-1} Å^{-2})	3349.44			1674.72			1674.72		
b_{ij}^0 (Å)	1.0990			1.4712			1.5065		
bond angles	HCH	aHCC[a]	cHCC[a]		HCR	aCCC[a]	cCCC[a]	CCR	RCR[b]
c_{ijk}^θ (kJ mol^{-1} rad^{-2})	164.96	199.29	199.29		199.29	302.29	302.29	302.29	302.29
θ_{ijk}^0 (rad)	1.9216	1.9190	1.8863		1.9246	1.8778	1.9380	1.9465	2.0559
torsion angles	RCCC			CCCC			CCCR		
c_{ijkl}^φ (kJ/mol)	11.723			11.723			11.723		

[a] Prefix "a" ("c") in aHCC and aCCC (cHCC and cCCC) denotes that the central atom in the bond angle is an achiral (chiral) carbon. [b] The c_{ijk}^θ and θ_{ijk}^0 given for the RCR bond angle were used only at the chain ends, since the iPP chains simulated were of the form R−CHR−(CH$_2$−CHR−)$_{x-1}$R, with x = 76 denoting the degree of polymerization.

Table 2. Simulation Parameters for Nonbonded Interactions

	HH	HC	HR	CC	CR	RR
			Local			
σ_{ij} (Å)	2.3160	2.7615	2.9400	3.2070	3.3855	3.5640
ϵ_{ij} (kJ/mol)	0.31925	0.33515	0.43054	0.35188	0.45188	0.58075
			Nonlocal			
σ_{ij} (Å)	2.5510	3.0422	3.1947	3.5333	3.6858	3.8383
ϵ_{ij} (kJ/mol)	0.18494	0.19498	0.26904	0.20544	0.28326	0.39121

The parameters for all bonded interactions mentioned above are borrowed from the work of Sylvester, Yip, and Argon[4] and are summarized here in Table 1.

The reader should note that, with the model and the parametrization used, the bonded geometry of iPP is strained at equilibrium. Thus, average values of bond lengths and bond angles depart significantly from the b_{ij}^0 and θ_{ijk}^0 values employed in the potential expressions of Table 1. In particular, the average length of a CC bond is 1.53 Å and the average value of an aCCC bond angle is 114°. The distributions of bond lengths and bond angles accumulated during the simulation at 400 K and 1 atm are given in the Supporting Information (S.M. Figure 1 and S.M. Figure 2).

As concerns the nonbonded interactions, all pairs of sites separated by more than two bonds along a chain or belonging to different chains interact through a Lennard-Jones (LJ) potential:

$$V_{ij}^{\mathrm{LJ}}(r_{ij}) = 4\epsilon_{ij}\left\{\left(\frac{\sigma_{ij}}{r_{ij}}\right)^{12} - \left(\frac{\sigma_{ij}}{r_{ij}}\right)^{6}\right\} \tag{4}$$

with r_{ij} being the scalar minimum image distance between interaction sites i and j. A systematic effort was undertaken to improve the representation of the nonbonded interactions. The methodology followed was very similar to that introduced in refs 6, 7, and 24. Local intramolecular interactions (between interaction sites three or four bonds apart) are described by the same set[1] of σ_{ij} and ϵ_{ij}, while a different set is used for nonlocal and intermolecular interactions.[6] The sets of σ_{ij} and ϵ_{ij} parameters used for local and nonlocal interactions are listed in Table 2. Lorentz−Berthelot combining rules have been adopted for both sets of σ_{ij} and ϵ_{ij} parameters.

Potential tails are cut at $1.45\sigma_{ij}$ and brought smoothly to zero at $2.33\sigma_{ij}$ using a quintic spline potential form.[1] Long-range attractions between atomic pairs are accounted for by direct integration of the LJ potentials, assuming radial distribution functions of 1 at separations greater than $1.45\sigma_{ij}$.

The simulation runs were conducted in the isobaric−isothermal (*NPT*) statistical ensemble, using the Nosé−Hoover[25,26] extended ensemble technique for maintaining both temperature and pressure fixed at their prescribed values. Simulations were performed at pressures P ranging from 1 to 1000 atm and temperatures T ranging from 450 to 650 K.

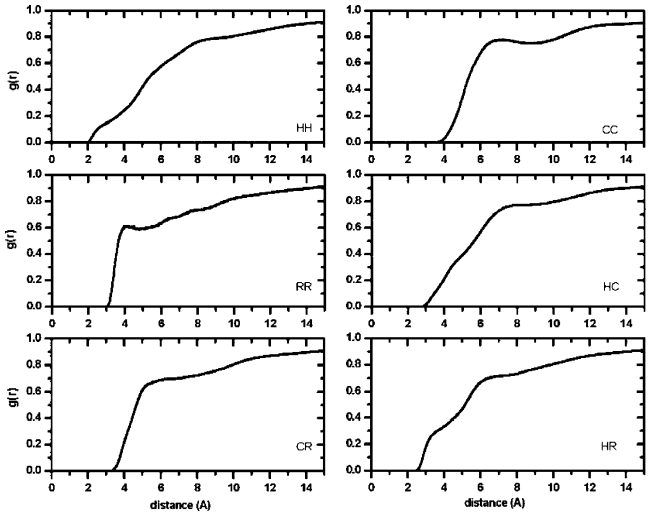

Figure 1. Intermolecular pair distribution functions $g(r)$ at T = 450 K and P = 1 atm.

Newton's equations of motion for all the interaction sites were integrated by means of a multiple time step velocity-Verlet algorithm. The fast degrees of freedom (bonded interactions: bond stretching, angle bending, and torsional oscillations) are integrated with a time step dt equal to 1 fs, whereas the slow degrees of freedom (nonbonded interactions) are integrated with a longer time step Δt = 2 dt. All MD runs were carried out with the large-scale atomic/molecular massively parallel simulator (LAMMPS) code.[27]

The initial configurations were equilibrated for 100−1000 ps, depending on the simulation conditions. Stabilization of the running average for the density and the various components of the energy was used as a criterion for starting saving the simulation trajectories. Configurations from the production phase of each simulation were recorded every 10 fs in order to track the fast motions which dominate the short-time segmental dynamics. Properties were obtained from analysis of 1−75 ns long trajectories, depending on the characteristic times associated with their equilibration.

3. Results

All results presented in the following sections are extracted from simulations conducted using the 2-molecule system, except for those of section 3.4.3, which were extracted from simulations conducted using the 16-molecule system.

3.1. Structural Properties. In order to comment on the structural properties of the iPP melts, the intermolecular pair distribution function $g(r)$, which is illuminating as regards intermolecular correlations and packing in the bulk, was calculated for all pairs of interaction sites present in the system. Representative plots for the $g(r)$ curves are shown in Figure 1.

The presence of the "correlation hole effect" is evident in the figure; at radial distances smaller than the radius of gyration

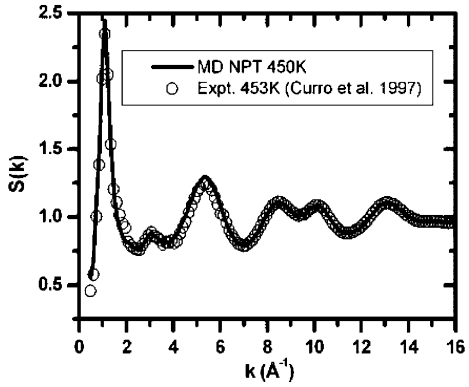

Figure 2. Simulated and experimental X-ray diffraction patterns of iPP near 450 K. The experimental measurements were performed by Curro et al.[28]

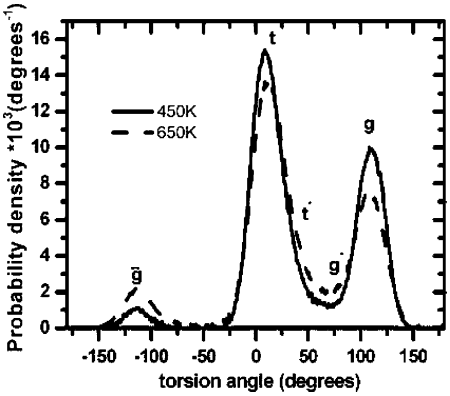

Figure 4. Simulated torsion angle distributions in iPP melt. Results were obtained from *NPT* simulations at 450 K (solid line), 650 K (dotted line), and atmospheric pressure. Also marked in the figure are the rotational isomeric states.

(see below, Table 6), $g(r)$ is suppressed relative to 1, since the cloud of segments belonging to the same chain as the reference segment excludes segments of other chains from getting closer to the reference segment.

The peaks in $g(r)$ reflect positions of intermolecular neighbors. The location of the first coordination shell for the RR pair appears to have moved toward closer distances in comparison with CC and CR pairs. The above observation can be explained by the fact that C atoms belong to the main backbone, whereas methyl groups (R) are pendant atoms. Skeletal carbons are kept apart by the substituents surrounding them, in contrast to the methyl groups, which are more exposed to neighboring sites and can approach each other at lower distances.

Comparing our results to analogous results of Antoniadis et al.,[7] we find that the two sets of plots are in a very good agreement. Available in the Supporting Information are the plots of the intermolecular pair distribution functions at $T = 450$ K and $P = 1$ atm out to distances of 40 Å, where the asymptotic value of 1 has been reached; those were extracted from simulations conducted using the 16-molecule system.

As a check of the correctness of structural predictions of the MD simulations, the static structure factor $S(k)$ was extracted from the $g^{\mathrm{tot}}(r)$ functions. This can be compared directly against experimental X-ray diffraction patterns.[28] $S(k)$ was calculated from the Fourier transforms of the total pair distribution functions. For a given wave vector **k**

$$S(k) = 1 + \frac{\left\langle \frac{1}{V} \right\rangle \sum_a \sum_b N_a N_b f^a(k) f^b(k) \int [g^{\mathrm{tot},ab}(r) - 1] \mathrm{e}^{-i\mathbf{k}\cdot\mathbf{r}} \, \mathrm{d}^3 r}{\sum_a [f^a(k)]^2} \quad (5)$$

In eq 5 $g^{\mathrm{tot},ab}(r)$ stands for the total pair distribution function between group types a and b. N_a and $f^a(k)$ are the total number of groups of type a in the model system and their atomic scattering factor, respectively. V is the model system volume. All six types of group pairs (HH, HC, HR, CC, CR, RR) were considered for the calculation of $S(k)$. The "atomic" scattering factors for H, C, and R were calculated through an analytical approximation described in ref 29, following a procedure similar to that of refs 6 and 7. The plot of $S(k)$ obtained from simulations at $T = 450$ K is shown in Figure 2, along with an experimentally obtained curve at $T = 453$ K.

The position and magnitude of the major intermolecular sharp peak near 1.1 Å^{-1} and of the intramolecular broader peaks near 3 and 5 Å^{-1} demonstrate good agreement with experimentally measured data. This agreement supports that the structure of the simulated polymer is realistic.

3.2. Conformational Properties. The five rotational isomeric states (RIS) for iPP according to Suter and Flory (t, g, $\bar{g}$, t^*, g^*), as defined in ref 30, are shown in Figure 3. The distribution of the torsion angles at two different temperatures, 450 and 650 K, was accumulated to investigate the conformations adopted by our system (see Figure 4). The five rotational isomeric states are also indicated in the figure.

The torsion angles display a continuous distribution with discernible peaks near the t, g, and $\bar{g}$ states. The t state is the most populated. The t^* and g^* states cannot be clearly detected; the former is completely merged with the t state, and the latter appears as a raised baseline between the dominant t and g peaks. Increasing the temperature causes a broadening and lowering of the peaks, as the system samples less energetically favorable states. The fractional populations for each state as a function of temperature for the 5-state model are listed in Table 3. In assigning bond angles to discrete rotational states, we followed the conventions of ref 1.

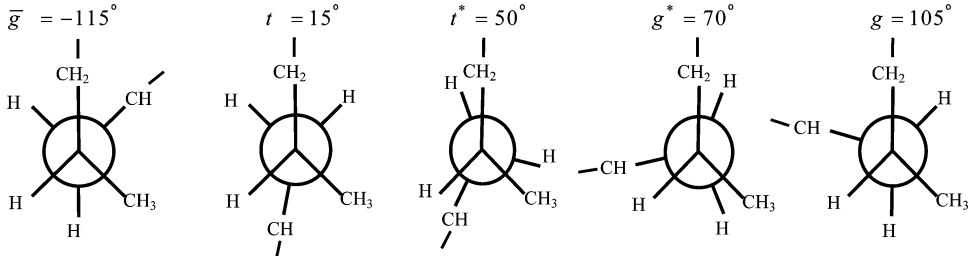

Figure 3. Rotational isomeric states trans (t, t^*) and gauche (g, $\bar{g}$, g^*).

Table 3. Fractional Populations of Rotational States in the Five-State Model, As Obtained from the Simulations

temp (K)	$\bar{g}$	t	t^*	g^*	g
450	0.045 ± 0.006	0.504 ± 0.004	0.100 ± 0.003	0.053 ± 0.001	0.297 ± 0.007
650	0.080 ± 0.001	0.469 ± 0.001	0.125 ± 0.001	0.071 ± 0.001	0.243 ± 0.002

A more detailed analysis of the distribution of torsional states adopted by *pairs* of adjacent bonds has been performed. Results from the simulation have been compared[31] against predictions from both the five-state RIS model of Suter and Flory[30] and an earlier, simpler three-state model.[32−35] These calculations and comparisons are presented in the Supporting Information accompanying this article. Agreement between simulations and the five-state RIS model is good, taking into account that the assignment of discrete rotational states to the torsion angles from the simulation is subject to considerable uncertainty. In general, the simulation gives a higher population of t and a lower population of g relative to the RIS models.

3.3. Volumetric Properties and Cohesive Energy Density. The parameters used for the nonbonded, nonlocal interactions in our model were calibrated by comparing the volumetric properties extracted from the MD simulation runs with available experimental data.[36,37] With the initial set of parameters used, the predicted density was systematically higher than the available experimental data. This observation pointed out the necessity of scaling the nonbonded, nonlocal LJ parameters. The strategy for extracting the modified σ_{ij} and ϵ_{ij} values is similar to that used in ref 24. The length parameters σ_{ij} of the LJ potential were first optimized by multiplying σ_{ij} for all i and j pairs with the same constant factor without modifying ϵ_{ij} parameters. Optimization of the ϵ_{ij} parameters followed. The optimization process was considered complete when the derived melt densities were found in good agreement with the available experimental data. The reader should bear in mind that, throughout the optimization procedure, the local parameters were kept fixed. Figure 5 shows how the specific volume of the optimized model varies with temperature; also shown are experimental values reported for iPP melts.

The calibrated parameters afford very good agreement between the simulation prediction and the experimental values. Thermodynamic properties such as the isobaric thermal expansivity, isothermal compressibility, and Hildebrand's solubility parameter were also evaluated and compared with available experimental data. The isobaric thermal expansivity was estimated through the expression

$$a_P = \frac{1}{\langle V\rangle}\frac{\Delta\langle V\rangle}{\Delta T}\Big)_P \tag{6}$$

by numerical differentiation of the $\langle V\rangle(T)$ predictions. The isothermal compressibility was calculated through the expression

$$\kappa_T = -\frac{1}{\langle V\rangle}\frac{\Delta\langle V\rangle}{\Delta P}\Big)_T \tag{7}$$

by numerical differentiation of the $\langle V\rangle(P)$ predictions. The solubility parameter was obtained through the expression

$$\delta = \sqrt{\frac{E_{\mathrm{coh}}}{\langle V\rangle}} \tag{8}$$

where the cohesive energy, E_{coh}, was estimated as the ensemble-averaged potential energy difference between the parent chains and the simulation box.[1] The simulation values, the experimental values, and the simulation conditions are shown in Table 4. The experimental predictions for a_P and κ_T are taken from the work of Sato et al.[37] and for δ from the work of Maier et al.[36]

3.4. Dynamical Properties. Important data from ^{13}C NMR, quasi-elastic neutron scattering (QENS), and dielectric spectroscopy (DS) experiments on isotactic polypropylene melts can be found in the literature from many different sources.[38−41] It is therefore significant to compare our simulation results on dynamical properties with these data.

3.4.1. Segmental Dynamics. Segmental dynamics of iPP melts was investigated through the reorientation of the methylene C−H bonds, as expressed by the second-order correlation function

$$P_2(t) = \frac{1}{2}\{3\langle[\mathbf{u}_{\mathrm{CH}}(t)\cdot\mathbf{u}_{\mathrm{CH}}(0)]^2\rangle - 1\} \tag{9}$$

where $\mathbf{u}_{\mathrm{CH}}(t)$ is the unit vector along a C−H bond at time t. The C−H bond vector orientation autocorrelation functions computed can be described well by the modified Kohlrausch−Williams−Watts (mKWW) function:[19]

$$P_{\mathrm{mKWW}}(t) = a\exp\left[-\left(\frac{t}{\tau_0}\right)\right] + (1-a)\exp\left[-\left(\frac{t}{\tau_{\mathrm{KWW}}}\right)^{\beta}\right] \tag{10}$$

The preceding mKWW function consists of two parts. The first term describes a fast exponential decay with amplitude a, which is associated with the librations of torsion angles around skeletal bonds and with the bond and bond angle bending vibrations of skeletal and pendant bonds near their equilibrium values, with characteristic time τ_0. The second term is a slower stretched exponential (KWW) decay associated with cooperative conformational transitions in the polymer, with τ_{KWW} being the characteristic correlation time and β the stretching exponent.

In the diagram of Figure 6 one can see the comparison between the second-order autocorrelation function extracted from simulation trajectories with the fitted mKWW functions. The mKWW provides an excellent fit to our simulation data

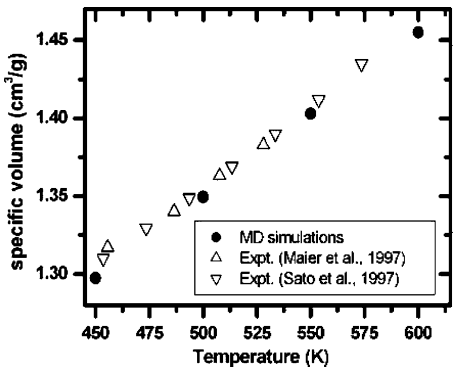

Figure 5. Temperature dependence of the specific volume as obtained from our MD simulation runs at $P = 1$ atm (filled circles). Also shown are available experimental data (open symbols) taken from refs 36 and 37.

Table 4. Thermodynamic Properties of iPP Melt[a]

property	conditions	simulation prediction	experimental value
$\alpha_P = \Delta\langle V\rangle/(\langle V\rangle\Delta T)$	$T = 450$, 600 K $P = 0.1$ MPa	$(7.5 \pm 0.1) \times 10^{-4}$ K^{-1} [a]	7.6×10^{-4} K^{-1} [a]
$\kappa_T = -\Delta\langle V\rangle/(\langle V\rangle\Delta P)$	$T = 500$ K $P = 0.1$, 10 MPa	$(1.8 \pm 0.3) \times 10^{-3}$ MPa^{-1} [a]	1.6×10^{-3} MPa^{-1} [a]
$\delta = (E_{coh}/\langle V\rangle)^{1/2}$	$T = 475$ K $P = 10$ MPa	14.8 ± 0.2 MPa$^{1/2}$	15.1 MPa$^{1/2}$

[a] The simulation prediction and the experimental value refer to (a) the thermal expansivity at T = 525 K, $P = 0.1$ MPa and (b) the isothermal compressibility at T = 500 K, $P = 5.05$ MPa.

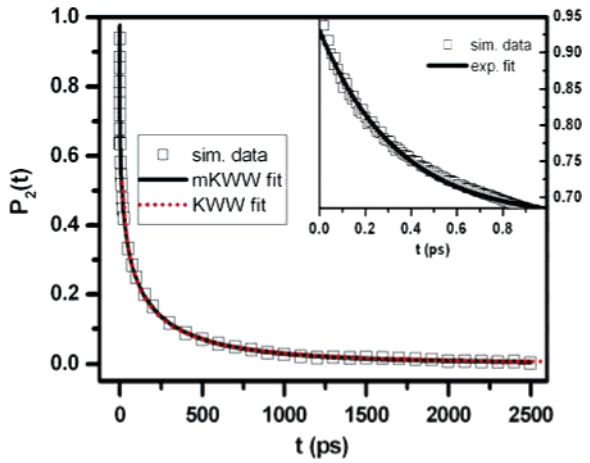

Figure 6. Time dependence of the $P_2(t)$ orientation autocorrelation function for C−H vectors calculated at 450 K and 1000 atm. Also shown is its analytical approximation with a stretched exponential function (dotted red line) for long times. The solid line indicates a modified stretched exponential (mKWW) function, which fits both regimes. Inset shows exponential fit at short times.

over the whole time range. In the plot is also shown a single-exponential fit, which captures the dynamics in the region $t \leq 1$ ps satisfactorily (fast dynamics). In the region $t > 1$ ps, where the decay is broader (slower dynamics), the simulation curve is well described by a mere stretched exponential[10] (KWW) function of the form

$$\mathrm{KWW}(t) = (1 - a)\exp\left[-\left(\frac{t}{\tau_{\mathrm{KWW}}}\right)^{\beta}\right] \qquad (11)$$

3.4.2. Effect of Pressure and Temperature on Segmental Dynamics. We have investigated the effect of pressure and temperature on the segmental dynamics, as expressed through the reorientation of the methylene C−H bonds by the second-order correlation function $P_2(t)$. The relaxation of the $P_2(t)$ curves, as obtained from our MD simulation runs at three different temperatures and three different pressures, is shown in Figures 7 and 8. The former shows the decay of $P_2(t)$ for three different temperatures at fixed pressure, while the latter displays the decay of $P_2(t)$ for three different pressures at constant temperature. The simulation results show how the curves decay in time as a function of temperature and pressure. The diagram supports that, as the temperature increases or the pressure decreases, the decay of $P_2(t)$ to zero is accelerated. Also shown are the best mKWW fits to the simulation data.

It can be further observed from the evolution of the $P_2(t)$ curves with time, shown in detail in Figure 7, that a rise in temperature of 100 K results in significant acceleration of the decay to zero for all studied pressures. The effect of pressure, on the other hand, which is shown in Figure 8, is not obvious for the change from 1 to 100 atm; the data practically coincide at these two pressure levels, even though the latter levels differ by 2 orders of magnitude. For a pressure rise from 100 to 1000 atm, a change of only 1 order of magnitude, the segmental relaxation rate is slowed down significantly. Both the effects of temperature and pressure can be explained in terms of the density of the system studied. As temperature changes by 100 K at constant pressure, density changes almost linearly with temperature. As pressure varies from 1 to 100 atm the density change is very small, so the dynamics is not significantly altered. However, as the pressure is raised further from 100 to 1000

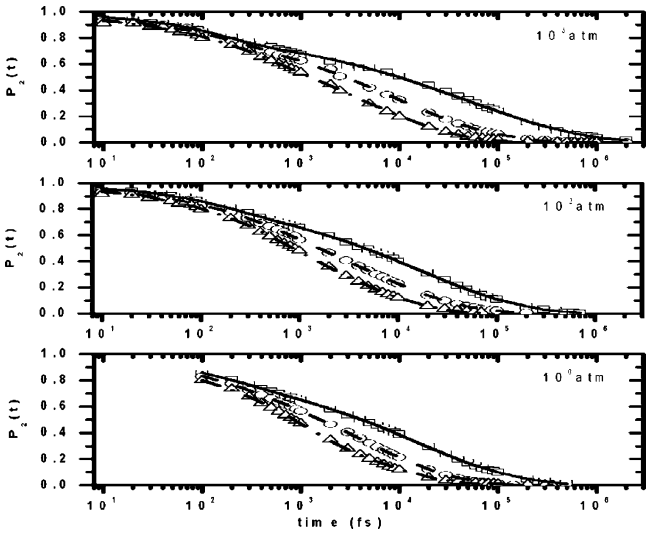

Figure 7. Time dependence of the $P_2(t)$ orientation autocorrelation function for C−H vectors, for three different temperatures and three different pressures. Rectangles indicate data at 450 K, ellipses data at 550 K, and triangles at 650 K. Curves are mKWW fits to the simulation results.

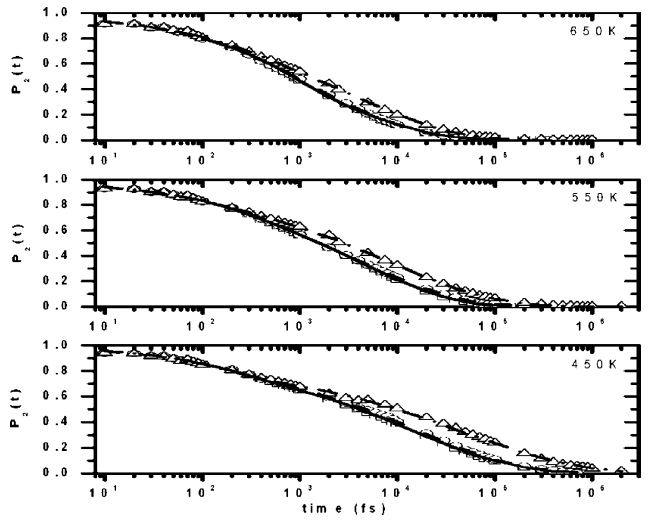

Figure 8. Time dependence of the $P_2(t)$ orientation autocorrelation function for C−H vectors, for three different pressures at three different temperatures. Rectangles indicate data at 1 atm, ellipses data at 100 atm, and triangles at 1000 atm. Curves are mKWW fits to the simulation results.

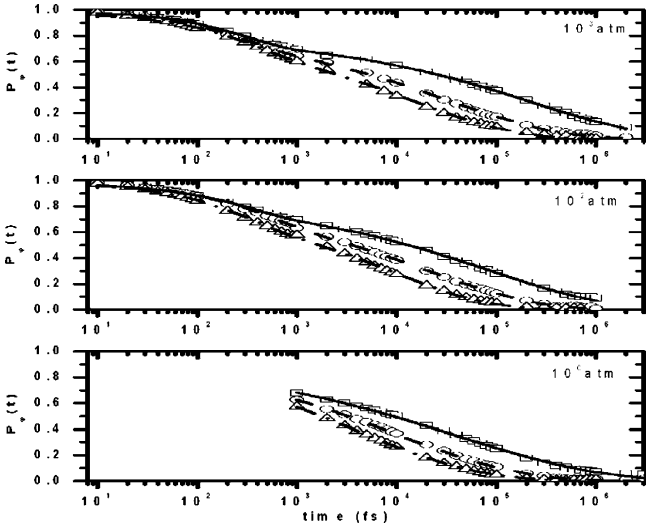

Figure 9. Time dependence of the $P_\phi(t)$ torsion angle autocorrelation function for three different temperatures at three different pressures. Rectangles indicate data at 450 K, ellipses data at 550 K, and triangles at 650 K. The lines are mKWW fits.

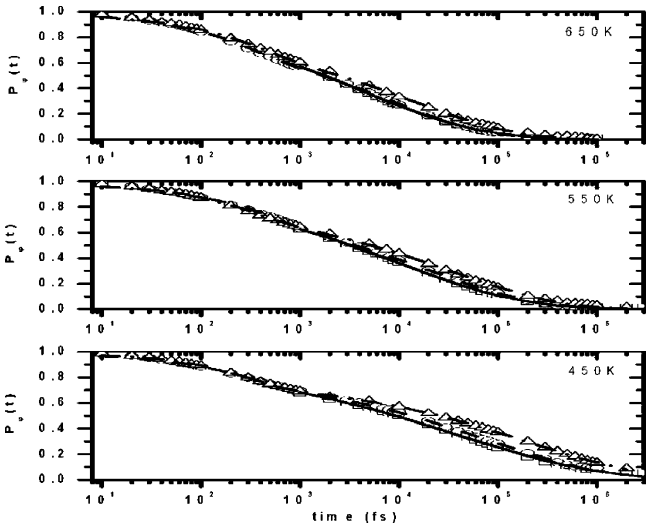

Figure 10. Time dependence of the $P_\phi(t)$ torsion angle autocorrelation function for three different pressures at three different temperatures. Rectangles indicate data at 1 atm, ellipses data at 100 atm, and triangles at 1000 atm. Curves are mKWW fits to the simulation results.

atm, the density difference is significant, a phenomenon that results in observable deceleration of the relaxation of the system. In addition, it is worth pointing out that the initial "exponentially decaying" part, associated with vibrations and librations, is affected little by temperature and almost not at all by pressure, in contrast to the "cooperative" KWW (α relaxation) part, which requires conformational isomerizations and is affected drastically.

The local dynamics of iPP melts, in particular their torsional dynamics, can be quantified through the torsion autocorrelation function, defined as

$$P_\phi(t) = \frac{\langle \cos(\phi(t))\cos(\phi(0))\rangle - \langle \cos(\phi(0))\rangle^2}{\langle \cos(\phi(0))\cos(\phi(0))\rangle - \langle \cos(\phi(0))\rangle^2} \quad (12)$$

where $\phi(t)$ is a nonterminal torsion angle at time t. The relaxation of the $P_\phi(t)$ curves, as obtained from our MD simulation runs at three different temperatures and three different pressures, is shown in Figures 9 and 10. The conclusions that can be drawn from these plots are similar to these that were already noted in

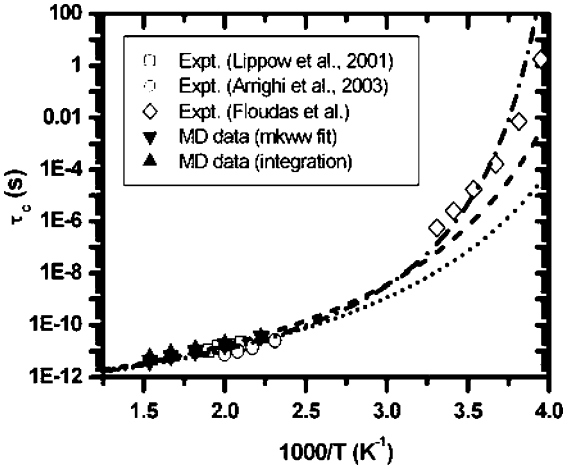

Figure 11. Temperature dependence of simulated and experimental mean correlation times at atmospheric pressure. MD simulation data were calculated from the mKWW fits to the C−H orientation autocorrelation function and from direct integration of the autocorrelation function (filled symbols). Experimental data are from NMR measurements (Lippow et al.),[38] QENS measurements at $q = 1$ Å^{-1} (Arrighi et al.),[39] and DS measurements (Floudas et al.).[40] Also indicated in the figure are VFT functions with parameters taken from ref 38 (dashed line) and ref 39 (dotted line) and a WLF function with parameters taken from ref 41 (dash-dotted line).

connection with the second-order correlation function $P_2(t)$. The increase of temperature or the decrease of pressure results in an acceleration of the decorrelation of the system.

At low temperatures and high pressures a change in the shape of the decorrelation functions is evident. The relaxation originates from two overlapping processes: a fast process occurring in the picosecond time scale, associated with the librations of torsion angles around skeletal bonds and with the bond and bond angle bending vibrations of skeletal and pendant bonds (β relaxation), and a slower process associated with cooperative conformational transitions in the polymer (α relaxation). This change in shape is due to the split of the α from the more localized β relaxation because of their different dependence on simulation conditions, which is more pronounced in lower temperature (and higher pressure) data. As temperature decreases (or pressure increases) the backbone starts to freeze; consequently, α relaxation becomes slower, whereas, on the other hand, β relaxation is relatively unaffected. This separation has also been observed in simulations of PE melts.[42]

The area under $P_2(t)$ defines the correlation time τ_C for C−H bond reorientational motion:

$$\tau_C = \int_0^\infty P_2(t)\,dt \quad (13)$$

With the observation that the mKWW function $P_{mKWW}(t)$ provides an excellent fit to $P_2(t)$, the mean correlation times of CH bond orientational relaxation are derived analytically using eqs 13 and 10 as

$$\tau_C = \int_0^\infty P_2(t)\,dt = \int_0^\infty P_{mKWW}(t)\,dt = a\tau_0 + (1-a)\tau_{KWW}\frac{1}{\beta}\Gamma\left(\frac{1}{\beta}\right) \quad (14)$$

The correlation time is plotted against inverse temperature in Figure 11. Two sets of simulation results are given as filled symbols. One set has been obtained by direct numerical integration of the $P_2(t)$ function computed from the simulation (eq 13). The second set has been obtained by the analytical representation of $P_2(t)$ consisting of the mKWW function (eq

Table 5. Parameters Used for the Fits of WLF and VFT Curves

VFT curve: $\log \tau_{seg} = \log \tau_{seg,\infty} + B/(T - T_0)$				WLF curve: $\log \tau(T) = \log \tau(T_g) - [C_1(T - T_g)]/[C_2 + (T - T_g)]$				
source	$\log(\tau_{seg,\infty}/s)$	T_0 (K)	B (K)	source	$\tau(T_g)$ (s)	T_g (K)	C_1	C_2 (K)
ref 38	−12.7	196	585	ref 41	100	255	14.5	30
ref 39	−12.7	186	554					

14).[10] The deviation between the two sets of results provides a measure of the accuracy with which τ_C can be computed from simulation. Also in Figure 11 are presented experimental measurements derived from ^{13}C NMR,[38] QENS,[39] and dielectric spectroscopy.[40] The lines through the simulation and experimental points in Figure 11 are the Vogel−Fulcher−Tamman (VFT)[38,39] and Williams−Landel−Ferry (WLF)[41] curves determined by experimental techniques, which show the dependence of relaxation times on temperature as the melt is cooled, approaching the glass transition temperature. The parameters used for the fits of WLF and VFT curves are listed in Table 5. Clearly, all sets of data are in reasonable agreement.

The relaxation times for C−H reorientational motion are discussed in further detail in two representations: $\tau_C(T,P$:const) and$\tau_C(P,T$:const), which provide complementary information.[21,43−45]

The temperature dependence of the correlation times was examined by plotting the simulation data, obtained under isobaric conditions, versus inverse temperature. Figure 12 clearly illustrates that the dependence for the three sets of data is described by the VFT equation:

$$\log \tau_C = \log \tau_0 + \frac{B}{T - T_0} \tag{15}$$

where $\log \tau_0$ is the limiting value at high T, B is the apparent activation energy, and T_0 is the "ideal" glass transition temperature.

The pressure dependence of the correlation times for the segmental dynamics was studied by plotting the simulation data, obtained under isothermal conditions, versus pressure. Within the investigated pressure range, as shown in Figure 13, the logarithms of the correlation times exhibit a linear dependence on P

$$\log \tau_C = \log \tau_0 + \Lambda(T)(P - P_0) \tag{16}$$

where τ_0 is the characteristic time at pressure P_0 and $\Lambda(T)$ is independent of pressure and is proportional to the activation volume for the motion. This kind of behavior has been observed for DS measurements on polyisoprene[43] and *cis*-polybutadiene.[45]

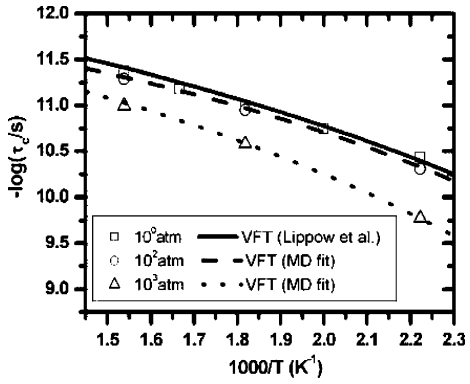

Figure 12. Temperature dependence of correlation times for three different pressures. The 1 atm MD predictions are compared directly with the VFT function fitted to NMR relaxation data of Lippow et al.[38] The lines for 100 and 1000 atm are fits of the VFT equation to the data for the available pressures.

If the relaxation process is considered as involving an activation volume ΔV (difference between the molar volumes of the activated and initial states), then ΔV can be extracted from $\Delta V = 2.303RT(\partial \log \tau_C/\partial P)_T$. From the slopes of the fits of $\log \tau_C$ vs P, the activation volume was calculated as 52.1 ± 0.97, 42.8 ± 3.34, and 44.95 ± 1.72 cm^3/mol at 450, 550, and 650 K, respectively. According to MD simulations, the calculated values of activation volume indicate that as the temperature decreases ΔV increases, consequently the number of monomers involved in the relaxation process increases. The same conclusion was reached via DS measurements on polyisoprene[43] and *cis*-1,4-polybutadiene.[45]

The T and P effects on the correlation times can be compared by plotting τ_C as a function of density.[21,46] This was done by collecting the correlation times measured under isobaric $\tau_C(T,P$:const) and isothermal $\tau_C(P,T$:const) conditions and is shown in Figure 14.

Through the observation of Figure 14 it is clear that the change of relaxation times under isobaric conditions is stronger than the one under isothermal conditions. From the data plotted in Figure 14 we were able to calculate the ratio of the activation

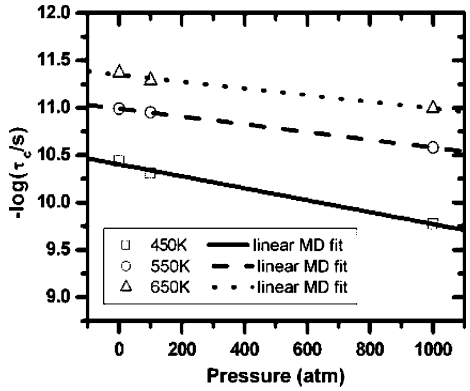

Figure 13. Pressure dependence of relaxation times for three different temperatures. The lines are linear fits to the data for the available temperatures.

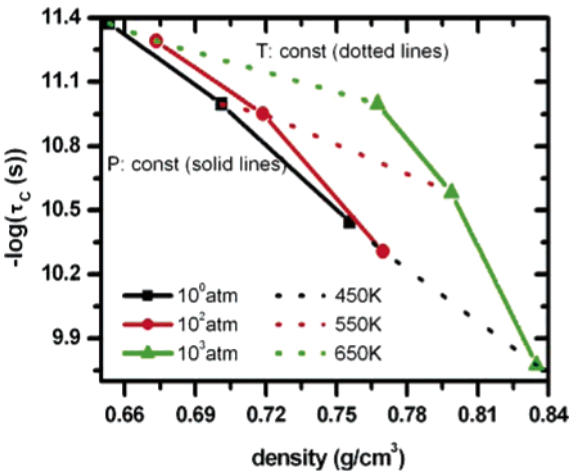

Figure 14. Relaxation times as a function of density. Solid lines correspond to relaxation times measured under isobaric conditions by changing the temperature; dotted lines correspond to relaxation times measured isothermally.

Table 6. Mean-Square End-to-End Distance, Radius of Gyration, Their Ratio, Their Fourth Moments, the Mean-Square Skeletal C−C Bond Length, and the Characteristic Ratio for Two Temperatures Studied

	$T = 450$ K	$T = 650$ K
$\langle R_E^2 \rangle$ (Å^2)	1894.28 ± 85.84	1873.14 ± 50.33
$\langle s^2 \rangle$ (Å^2)	297.46 ± 8.98	300.46 ± 5.14
$\langle R_E^2 \rangle / \langle s^2 \rangle$	6.37 ± 0.35	6.23 ± 0.20
$\langle R_E^4 \rangle / \langle R_E^2 \rangle^2$	1.435 ± 0.024	1.490 ± 0.015
$\langle s^4 \rangle / \langle s^2 \rangle^2$	1.147 ± 0.011	1.157 ± 0.005
$\langle l^2 \rangle$ (Å^2)	2.27 ± 0.09	2.28 ± 0.12
C_n	5.49 ± 0.33	5.41 ± 0.32

energy at constant volume E_V^* over the enthalpy of activation H^*. This ratio is defined as

$$\frac{E_V^*}{H^*} = 1 - \left(\frac{\partial P}{\partial T}\right)_V \left(\frac{\partial T}{\partial P}\right)_\tau = 1 - \frac{(\partial \rho/\partial T)_P (\partial \ln \tau/\partial P)_T}{(\partial \rho/\partial P)_T (\partial \ln \tau/\partial T)_P} = 1 - \frac{(\partial \ln \tau/\partial \rho)_T}{(\partial \ln \tau/\partial \rho)_P} \quad (17)$$

and provides a quantitive measure of the relative importance of P and T on the dynamics. The value of the E_V^*/H^* ratio calculated is 0.54 ± 0.08, a value indicating that the temperature provides the main means of affecting the dynamics. It is suggested in the literature that the degree of packing, which is reflected by the broad scattering peaks in the wide-angle X-ray pattern, and the dynamic quantity E_V^*/H^* are correlated.[46] For glass-forming polymers with $q^* < 5$ nm^{-1}, where q^* is the position of the first peak in the X-ray pattern, the ratio is below 0.6, and for glass formers with $q^* > 15$ nm^{-1} the ratio is higher than 0.6. We justify the above experimental conclusions, since both the first peak of iPP (11 nm^{-1}) and the extracted value of the ratio are positioned in the intermediate regime between the above regions.

3.4.3. Chain Dynamics. The results presented in this section are based on simulations where the bigger system of 16 molecules was used, in order to avoid system size effects and to have better statistics in the calculations.

The equilibrium values of $\langle s^2 \rangle$, $\langle R_E^2 \rangle$, and the value of their ratio for the two temperature studied are presented in Table 6. The time required for equilibration for $\langle R_E^2 \rangle$ at $T = 450$ and 650 K is around 57 and 15 ns, respectively. From the equilibrium values of $\langle R_E^2 \rangle$, the characteristic ratio C_n (Table 6) was extracted, defined as

$$C_n = \frac{\langle R_E^2 \rangle}{2 n_m \langle l^2 \rangle} \quad (18)$$

where n_m is the number of monomers per chain and $\langle l^2 \rangle$ is the mean-square skeletal C−C bond length at equilibrium. The values reported in the literature based on small-angle neutron scattering measurements in the melt, rotational isomeric state (RIS) model calculations,[30] MD simulations[47] of single chains in a Θ solvent, and parallel tempering end-bridging Monte Carlo (EBMC) melt simulations with a somewhat different, partially constrained model[11] are equal to 6.2, 4.2, 6.1, and 6.6 ± 0.3, respectively.

The fourth moments of R_E and s were also evaluated (Table 6). Simulation values for these quantities, reduced by $\langle R_E^2 \rangle^2$ and $\langle s^2 \rangle^2$, respectively, are smaller than the values 5/3 and 19/15 expected of very long Gaussian chains.[31] Clearly, these values are subject to finite chain length effects in the simulated systems.

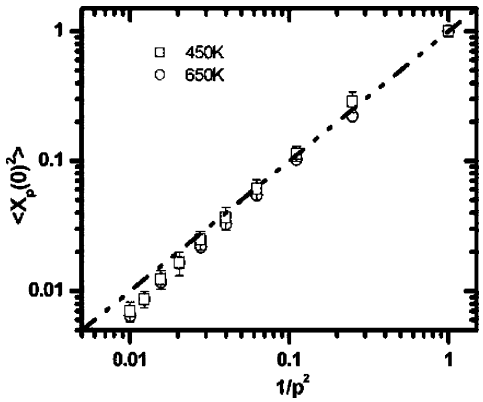

Figure 15. Square amplitudes of the Rouse normal modes $\langle \mathbf{X}_P(0)^2 \rangle$, normalized by the $\langle \mathbf{X}_1(0)^2 \rangle$, as a function of the inverse squared mode number for iPP melts at two different temperatures, $T = 450$ and 650 K. The line corresponds to the Rouse model prediction.

The Rouse model[48,49] has been remarkably effective in the description of chain dynamics of polymer melts, as long as their molecular weight is below the entanglement regime. The value of the entanglement molecular weight reported in the literature for iPP melts from Eckstein et al.,[50] by means of oscillatory rheometry, is 6900 g mol^{-1}, whereas the value estimated by Fetters et al.[51] is between 5100 and 5500 g mol^{-1}. The difference between the reported values is due to the factor (4/5) which is taken into account in the latter reference in the expression relating the entanglement molecular weight with the plateau modulus. Both values are considerably larger than the molar mass (3208 g mol^{-1}) of the melts simulated here.

The Rouse model considers a polymer chain as a sequence of N Brownian particles, numbered 0, 1, ..., $N - 1$, connected by harmonic springs (Gaussian model) and moving in a viscous medium representing the background environment formed by all other chains. The basic assumptions of the Rouse model allow treating the system through an analysis of normal modes $\mathbf{X}_p$, $p = 0, 1, 2, ..., N - 1$, each of which is capable of independent motion. The autocorrelation function of normal mode $\mathbf{X}_p$ is expressed as

$$\langle \mathbf{X}_p(t) \cdot \mathbf{X}_p(0) \rangle = \frac{\langle R_E^2 \rangle}{6\pi^2} \frac{1}{p^2} \exp\left(-\frac{t}{\tau_p}\right) \quad (19)$$

where $\{\tau_p\}$ denotes the spectrum of relaxation times $\tau_p = \tau_1/p^2$ with

$$\tau_1 = \tau_R = \frac{\zeta N \langle R_E^2 \rangle}{3\pi^2 k_B T} \quad (20)$$

being the longest relaxation time.

Figure 15 shows the mean-square amplitudes of the Rouse normal modes $\langle \mathbf{X}_p(0)^2 \rangle$, normalized by the amplitude of the first normal mode $\langle \mathbf{X}_1(0)^2 \rangle$, as a function of $1/p^2$, for two different temperatures, 450 and 650 K. According to the analysis of the Rouse model, eq 19, the dependence should be linear; this scaling is followed for the first six normal modes for both temperatures. As p increases, the subchain whose motion is described by the pth mode gets shorter and the Gaussian assumption postulated by the Rouse model breaks down.

The time evolution of the autocorrelation function for the first five Rouse normal modes extracted from the simulation runs (symbols) and their best exponential fits (lines) are plotted

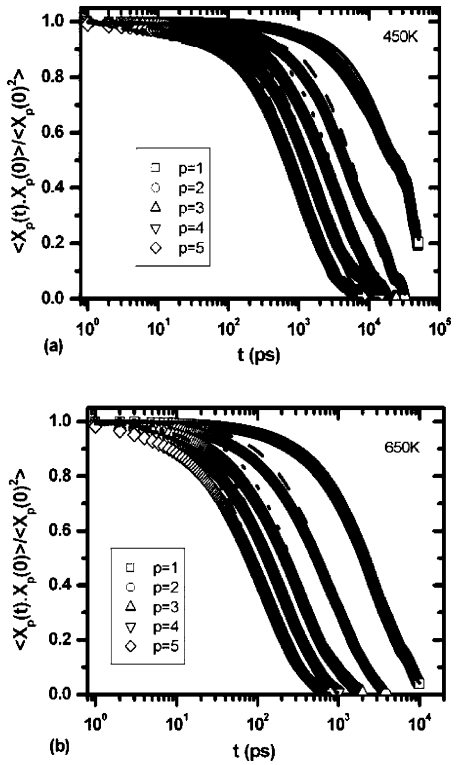

Figure 16. Time autocorrelation function for the first five Rouse normal modes (symbols) and their exponential fits (lines): (a) 450 K and (b) 650 K.

in Figure 16. By fitting the simulation results with an exponential function, estimates of the relaxation times τ_p were extracted (Table 7). The time decay is not exactly exponential in the short-time region, even though the first five normal modes are superposable, within simulation error, when scaled according to the Rouse model. The time decays of the modes follow the Rouse model prediction in the long-time region. Similar behavior has also been observed in other simulations with both atomistic[18,19,23] and coarse-grained models.[22]

The zeroth normal mode $\mathbf{X}_0$ represents the chain center of mass position, with mean-square displacement defined as

$$\langle (R_G(t) - R_G(0))^2 \rangle = \frac{6k_BT}{N\zeta} t \tag{21}$$

Figure 17 shows the time evolution of the mean-square displacement of the chain centers of mass for 450 and 650 K.

The mean-square displacement of the center of mass displays a nonlinear dependence on time (anomalous diffusion) at short times (times smaller that the longest calculated relaxation time, $t < \tau_1$) for both sets of data. A non-Fickian, subdiffusive behavior is observed here, where the time evolution of the mean-square displacement of the center of mass exhibits a dependence $\sim t^{1/2}$. This kind of behavior has been observed in other simulations.[18,23,47] It is obvious that in the long time regime ($t \geq \tau_1$) the dependence of $\langle (R_G(t) - R_G(0))^2 \rangle$ on time is linear. Values of the self-diffusion coefficient D for two different temperatures are presented in Table 8, calculated from the long-

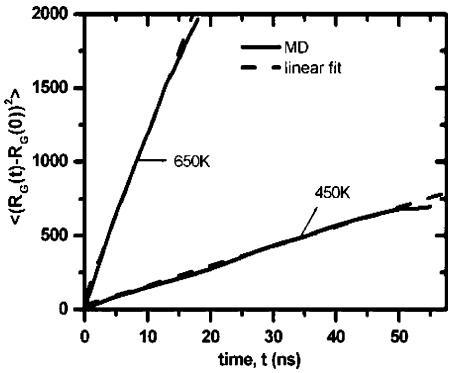

Figure 17. Time evolution of the chain center of mass mean-square displacement (solid lines) and its linear fit (dashed lines) for temperatures $T = 450$ and 650 K.

Table 8. Values for the Self-Diffusivity, the Friction Factor, and the Zero-Shear Viscosity vs Temperature

temp (K)	D (10^{-6} cm^2/s)	ζ_D (10^{-9} dyn/cm)	ζ_τ (10^{-9} dyn/cm)	η_0 (cP)
450	0.24 ± 0.01	1.74 ± 0.07	2.1 ± 0.1	19.9 ± 0.2
650	2.02 ± 0.12	0.29 ± 0.02	0.29 ± 0.01	2.98 ± 0.16

time behavior of the center of mass mean-square displacement using the Einstein relation

$$D = \lim_{t\to\infty} \frac{\langle (R_G(t) - R_G(0))^2 \rangle}{6t} \tag{22}$$

Combining eqs 21 and 22, one can extract an estimate of the friction factor ζ, which is an important parameter in the Rouse formulation, since it sets the time scale for the dynamics:

$$\zeta_D = \frac{k_BT}{ND} \tag{23}$$

An alternative estimate of the friction factor is obtainable from eq 20 for the Rouse time:

$$\zeta_\tau = 3\pi^2 \frac{k_BT}{N\langle R_E^2 \rangle} \tau_1 \tag{24}$$

Values of ζ_D and ζ_τ per skeletal carbon extracted from the simulations via eqs 23 and 24 are presented in Table 8. Estimates of the zero-shear viscosity of the melt can be extracted from the MD values of the self-diffusivity, as discussed in ref 18, using the Rouse model relation

$$\eta_0 = \frac{\rho RT}{36MD} \langle R_E^2 \rangle \tag{25}$$

The Rouse model predicts a relation for the relaxation of the time autocorrelation function of the end-to-end vector as

$$\frac{\langle R_E(t) \cdot R_E(0) \rangle}{Nb^2} = \sum_{p=1,3,5,\ldots} \frac{8}{\pi^2 p^2} \exp\left(-\frac{tp^2}{\tau_1}\right) \tag{26}$$

Figure 18 presents the time evolution of the autocorrelation function of the chain end-to-end vector for two temperatures.

Table 7. Values of the Relaxation Times of the Rouse Modes and Their Ratios

temp (K)	τ_1 (ns)	τ_2 (ns)	τ_3 (ns)	τ_1/τ_2	τ_1/τ_3
450	31.82 ± 1.07	7.88 ± 0.86	4.06 ± 0.34	4.11 ± 0.31	7.91 ± 0.41
650	3.074 ± 0.117	0.863 ± 0.14	0.365 ± 0.01	3.56 ± 0.84	8.40 ± 0.12

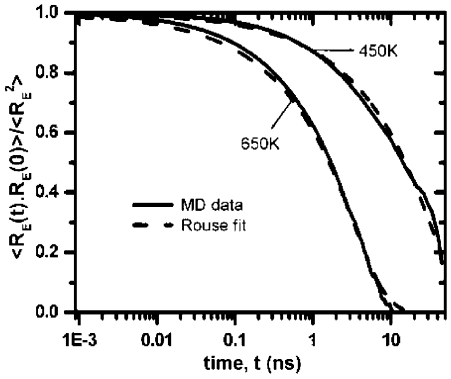

Figure 18. Time autocorrelation function for the chain end-to-end vector as calculated from the simulation (solid line) and fitted using the Rouse model analysis (dashed line) for temperatures $T = 450$ and 650 K.

The plot demonstrates clearly that, as the temperature increases, the relaxation time decreases, and the system needs sufficiently less time to decorrelate. In Figure 18 is also presented a comparison between the simulation results (solid line) and the relation predicted from the Rouse model with the friction factor ζ_D extracted above. The Rouse model analysis captures satisfactorily the slow decay at long times.

4. Conclusions

In this work we have presented results from atomistic molecular dynamics simulations in the isothermal−isobaric (*NPT*) ensemble for the structural, conformational, volumetric, and dynamical properties of iPP melts.

All simulations were performed using a molecular model in which polypropylene chains are represented in terms of explicit atoms, except for methyl groups which are represented as united atoms. The model is fully flexible, with bond lengths and bond angles subject to harmonic potentials and a 3-fold symmetric torsional potential associated with all nonterminal dihedral angles. The nonbonded potential distinguishes between local intramolecular and nonlocal intra- and intermolecular interactions.

The model developed was validated through comparisons of the volumetric and thermodynamic properties extracted from the MD simulations against available experimentally measured values. The structure of the simulated polymer melt was examined by calculating the X-ray diffraction pattern and comparing it with experiment. Both the positions and the magnitudes of the peaks in the diffraction pattern agree well with experiment, indicating that the simulated polymer structure is realistic.

Segmental dynamics has been investigated through the orientational autocorrelation functions of methylene C−H bonds and through the autocorrelation functions of torsion angles over a wide range of temperatures and pressures. The modified KWW expression, eq 10, provides an excellent fit to all simulation data over the whole range of times, both in the short time regime, where autocorrelation functions exhibit a fast exponential decay, and in the long time regime, where the decay is stretched. It was further observed from the evolution of the $P_2(t)$ and $P_\phi(t)$ curves with time that a rise in temperature by 100 K results in a significant acceleration of the segmental dynamics for all studied pressures under isobaric conditions. The effect of pressure on the segmental dynamics, on the other hand, is weaker and becomes obvious for a pressure change from 100 to 1000 atm, where appreciable change in the system density takes place.

Predicted correlation times for segmental dynamics agree reasonably well with different kinds of experimental data derived from ^{13}C NMR, QENS, and dielectric spectroscopy measurements. Segmental correlation times from the MD exhibit a VFT dependence on temperature as the melt is cooled at constant pressure approaching the glass transition temperature, T_g; the logarithm of the segmental correlation time was found to increase linearly with pressure under isothermal conditions. Furthermore, the temperature and pressure effects on the relaxation times were compared by examining the correlation time as a function of density under isothermal and isobaric conditions. It was concluded that the effect of temperature is stronger than that of pressure, the calculated value of the E_V^*/H^* ratio exceeding 0.5. From the slopes of the fits of log τ_C vs P, the activation volume for segmental motion was calculated; it was found to increase strongly as temperature decreases toward T_g. This indicates that the number of monomers involved in the segmental relaxation process increases with decreasing temperature.

Simulations were sufficiently long to equilibrate the overall conformational characteristics of chains. The characteristic ratio was extracted from the equilibrium values $\langle R_E^2 \rangle$ and found to agree reasonably well with available values from neutron diffraction and other calculations.

By systematically mapping the atomistic MD trajectories onto the Rouse model, dynamical behavior at the chain level was investigated. It was verified that long length scale chain dynamics can be described well by the Rouse model, through the normal-mode analysis. The dependence of the mean-square amplitudes of the Rouse normal modes $\langle \mathbf{X}_P(0)^2 \rangle$ on $1/p^2$ is found to be linear for the first five modes; for higher modes deviations from linearity are observed, as expected from the fact that the Gaussian model is inappropriate for short subchains. The spectrum of relaxation times τ_p was extracted from the decay of the autocorrelation functions of the five first modes. Values of the self-diffusion coefficient D were also extracted from the mean-square displacement of the chain centers of mass in the long-time, Einstein regime. Values of the segmental friction factor ζ were extracted from the Rouse time and from the self-diffusivity and used to estimate the zero-shear viscosity.

Acknowledgment. We gratefully acknowledge the General Secretariat of Research and Technology of Greece for the support in the form of a PENED 01, Program, 01EΔ529. We thank Professor George Floudas for making his DS results available to us prior to publication.

Supporting Information Available: Figures of simulated bond length and bond angle distributions in iPP melt and intermolecular pair distribution functions $g(r)$; tables of a priori probabilities of pairs of rotational states adopted by dyads. This material is available free of charge via the Internet at http://pubs.acs.org.

References and Notes

(1) Theodorou, D. N.; Suter, U. W. *Macromolecules* **1985**, *18*, 1467−1478.
(2) Mansfield, K. F.; Theodorou, D. N. *Macromolecules* **1990**, *23*, 4430−4445.
(3) Mansfield, K. F.; Theodorou, D. N. *Macromolecules* **1991**, *24*, 4295−4309.
(4) Sylvester, M. F.; Yip, S.; Argon, A. S. In *Computer Simulation of Polymers*, 1st ed.; Roe, R.-J., Ed.; Prentice Hall: Englewood Cliffs, NJ, 1991; p 105.
(5) Mansfield, K. F.; Theodorou, D. N. *Macromolecules* **1991**, *24*, 6283−6294.
(6) Antoniadis, S. J.; Samara, C. T.; Theodorou, D. N. *Macromolecules* **1998**, *31*, 7944−7952.

(7) Antoniadis, S. J.; Samara, C. T.; Theodorou, D. N. *Macromolecules* **1999**, *32*, 8635−8644.
(8) Ryckaert, J. P.; Arialdi, G.; Melchionna, S. *Mol. Phys.* **2001**, *99*, 155−165.
(9) Destrée, M.; Lauprêtre, F.; Lyulin, A.; Ryckaert, J. P. *J. Chem. Phys.* **2000**, *112*, 9632−9644.
(10) Ahumada, O.; Theodorou, D. N.; Triolo, A.; Arrighi, V.; Karatasos, C.; Ryckaert, J.-P. *Macromolecules* **2002**, *35*, 7110−7124.
(11) Theodorou, D. N. In *Bridging Time Scales: Molecular Simulations for the Next Decade*; Nielaba, P., Mareschal, M., Ciccotti, G., Eds.; Springer-Verlag: Berlin, 2002; pp 67−127.
(12) Doruker, P.; Mattice, W. L. *Macromol. Theory Simul.* **1999**, *8*, 463−478.
(13) Clancy, T. C.; Mattice, W. L. *J. Chem. Phys.* **2000**, *112*, 10049−10055.
(14) Xu, G.; Clancy, T. C.; Mattice, W. L. *Macromolecules* **2002**, *35*, 3309−3311.
(15) Clancy, T. C.; Mattice, W. L. *J. Chem. Phys.* **2001**, *115*, 8221−8225.
(16) Choi, P.; Mattice, W. L. *J. Chem. Phys.* **2004**, *121*, 8647−8651.
(17) Mattice, W. L.; Helfer, C. A.; Rane, S. S.; von Meerwall, E. D.; Farmer, B. L. *J. Polym. Sci., Part B: Polym. Phys.* **2005**, *43*, 1271−1282.
(18) Harmandaris, V. A.; Mavrantzas, V. G.; Theodorou, D. N. *Macromolecules* **1998**, *31*, 7934−7943.
(19) Doxastakis, M.; Theodorou, D. N.; Fytas, G.; Kremer, F.; Faller, R.; Müller-Plathe, F.; Hadjichristidis, N. *J. Chem. Phys.* **2003**, *119*, 6883−6894.
(20) Tsolou, G.; Mavrantzas, V. G.; Theodorou, D. N. *Macromolecules* **2005**, *38*, 1478−1492.
(21) Tsolou, G.; Harmandaris, V. A.; Mavrantzas, V. G. *J. Chem. Phys.* **2006**, *124*, 084906.
(22) Kremer, K.; Grest, G. S. *J. Chem. Phys.* **1990**, *92*, 5057.
(23) Paul, W.; Smith, G. D.; Yoon, D. Y. *Macromolecules* **1997**, *30*, 7772.
(24) Widmann, A. H.; Laso, M.; Suter, U. W. *J. Chem. Phys.* **1995**, *102*, 5761−5769.
(25) Nosé, S. *Prog. Theor. Phys. Suppl.* **1991**, *103*, 1−46.
(26) Hoover, W. G. *Phys. Rev. A* **1986**, *31*, 1695−1697.
(27) Plimpton, S. J. *Comput. Phys.* **1995**, *117*, 1−19.
(28) Curro, J. G.; Weinhold, J. D.; Rajasekaran, J. J.; Habenschuss, A.; Londono, J. D.; Honeycutt, J. D. *Macromolecules* **1997**, *30*, 6264−6273.
(29) Narten, A. H. *J. Chem. Phys.* **1979**, *70*, 299−304.
(30) Suter, U. W.; Flory, P. J. *Macromolecules* **1975**, *8*, 765−776.
(31) Mattice, W. L.; Suter, U. W. In *Conformational Theory of Large Molecules*; Wiley-Interscience: NewYork, 1994; pp 173−191.
(32) Flory, P. J. *J. Am. Chem. Soc.* **1966**, *89*, 1798−1804.
(33) Fujiwara, Y.; Flory, P. J. *Macromolecules* **1970**, *3*, 1798−1804.
(34) Biskup, U.; Cantow, H. *Macromolecules* **1972**, *5*, 546.
(35) Suter, U. W.; Pucci, S.; Pino, P. *J. Am. Chem. Soc.* **1975**, *97*, 1018−1023.
(36) Maier, R. D.; Thonmann, R.; Kressler, J.; Mülhaupt, R. *J. Polym. Sci., Polym. Phys.* **1997**, *35*, 1135−1144.
(37) Sato, Y.; Yamasaki, Y.; Takishima, S.; Masuoka, H. *J. Appl. Polym. Sci.* **1997**, *66*, 141−150.
(38) Lippow, S. M.; Qiu, X. H.; Ediger, M. D. *J. Chem. Phys.* **2001**, *115*, 4961−4965.
(39) Arrighi, V.; Batt-Coutrot, D.; Zhang, C.; Telling, M. T. F.; Triolo, A. *J. Chem. Phys.* **2003**, *119*, 1271−1278.
(40) Floudas, G., University of Ioannina, private communication.
(41) Zemke, K.; Schmidt-Rohr, K.; Spiess, H. W. *Acta Polym.* **1994**, *45*, 148−159.
(42) Arialdi, G.; Ryckaert, J.-P.; Theodorou, D. N. *Chem. Phys.* **2003**, *292*, 371−382.
(43) Floudas, G.; Resinger, T. *J. Chem. Phys.* **1999**, *111*, 5201−5204.
(44) Floudas, G.; Fytas, G.; Resinger, T.; Wegner, G. *J. Chem. Phys.* **1999**, *111*, 9129−9132.
(45) Floudas, G.; Gravalides, C.; Resinger, T.; Wegner, G. *J. Chem. Phys.* **1999**, *111*, 9847−9852.
(46) Floudas, G.; Mpoukouvalas, K.; Papadopoulos, P. *J. Chem. Phys.* **2006**, *124*, 074905.
(47) Ryckaert, J. P. In *Monte Carlo and Molecular Dynamics of Condensed Matter Systems;* Conference Proceedings Vol. 47; Binder, K., Ciccotti, G., Eds.; Società Italiana di Fisica: Bologna, 1996; Chapter 27, pp 729−746.
(48) Rouse, P. E. *J. Chem. Phys.* **1963**, *21*, 1272.
(49) Doi, M.; Edwards, S. F. *Theory of Polymer Dynamics*; Clarendon: Oxford, 1986.
(50) Eckstein, A.; Suhm, J.; Friedrich, C.; Maier, R. D.; Sassmannshausen, J.; Bochmann, M.; Mülhaupt, R. *Macromolecules* **1998**, *31*, 1335−1340.
(51) Fetters, L. J.; Lohse, D. J.; Graessley, W. W. *J. Polym. Sci., Part B: Polym. Phys.* **1998**, *37*, 1023−1033.

MA062234U